Geophys. J. Int. (2008) **173,** 827–843 doi: 10.1111/j.1365-246X.2008.03751.x

Azimuthal anisotropy of Rayleigh-wave phase velocities in the east-central United States

Frédéric Deschamps,[1,2] Sergei Lebedev,[2] Thomas Meier[3] and Jeannot Trampert[2]

[1]*Institut für Geophysik, Swiss Federal Institute of Technology, ETH Hönggerberg HPP* L8.1, 8093 *Zürich, Switzerland. E-mail: frederic.deschamps@erdw.ethz.ch*

[2]*Department of Earth Sciences, Utrecht University, Budapestlaan* 4, PO Box 80021, 3508 *TA Utrecht, The Netherlands*

[3]*Ruhr University Bochum, Universitätsstrasse* 150, NA3/165, 44780 *Bochum, Germany*

Accepted 2008 February 4. Received 2008 February 4; in original form 2006 November 6

SUMMARY

We explore the Rayleigh-wave phase velocity structure of the east-central US in a broad period range (10–200 s). Using a recent implementation of the two-stations method, we first measure interstation dispersion curves of Rayleigh-wave phase velocities along 60 paths. We then invert our collection of dispersion curves for isotropic and azimuthally anisotropic (2Ψ and 4Ψ) phase–velocity maps. The inversion is performed by a damped, smoothed LSQR, and the output model is parametrized on a triangular grid of knots with a 140 km grid spacing. Using the isotropic component of the phase velocity maps to constrain regional variations in shear velocity and Moho-depth, we observe that over the upper-middle crust depth range ($z < 30$ km) shear wave velocities are lower beneath the Grenville and Appalachian orogenic provinces than beneath the Central Plains to the west. The amplitude of (2Ψ) anisotropy and the azimuth of the fast-propagation direction at periods between 20 and 34 s vary laterally. Beneath the Grenville and Appalachian provinces, the amplitude of anisotropy reaches 1 per cent of the average phase velocity, and the azimuth of the fast-propagation direction is uniform and equal to 32°. West of the Grenville front, the average amplitude falls to 0.5 per cent, and the azimuth of the fast-propagation direction is less uniform. In the period range 45–60 s, anisotropy is smaller in amplitude (∼0.5 per cent) and with a regionally uniform azimuth of the fast-propagation direction of around 165°. Around 140 s, the amplitude of 2Ψ anisotropy is larger again (>1 per cent), and the azimuth of the fast-propagation direction is uniform over the entire region and equal to 54°. Our results suggest that azimuthal anisotropy beneath the east-central US is vertically distributed in three distinct layers, with a different geodynamic origin for each of them.

Key words: Surface waves and free oscillations; Seismic anisotropy; North America.

1 INTRODUCTION

Azimuthal anisotropy is of great interest to infer past and present deformation in the lithosphere and asthenosphere, and can be retrieved by studying either the polarization of seismic waves speeds (mainly SKS and S), or the azimuthal dependence of body or surface wave speeds. In one given region, lithospheric and asthenospheric deformations are often discussed as alternative origin for azimuthal anisotropy. Stratification of anisotropy, however, has increasingly been revealed by recent surface wave observations, sometimes combined with shear wave splitting data (e.g. Simmons *et al.* 2002; Smith *et al.* 2004; Sebai *et al.* 2006; Marone & Romanowicz 2007). In this paper, we build an anisotropic model of Rayleigh-wave phase velocity in the east-central US (31°N–41°N, and 82°E–92°E), and observe different azimuthal anisotropy patterns in three distinct period ranges, suggesting that in this region azimuthal anisotropy is vertically distributed in at least three layers.

The tectonics of the east-central US is dominated by the southern part of the Grenville and Appalachian orogenic belts. During the Grenville orogeny, which was active between 1.3 and 1.0 Gyr, small continents accreted to the Laurentia supercontinent (see Hoffman 1988 for a review; and Karlstrom *et al.* 2001, for a recent study). The southern portion of the Grenville front (thick curve in Fig. 1) runs southwestwards down to 34°N latitude, and bends westwards. The Appalachian front (thick dashed curve in Fig. 1) is associated with a more recent orogeny (350–300 Ma), during which Gondwana and North America collided (e.g. Ziegler 1989). It also runs southwestwards down to 32°N latitude, where it bends westwards (Ouachitas mountains). West of the Grenville front are the stable cratonic Central Plains. These terrains are believed to have experienced little or no tectonic activity during the past 1.6 Gyr (Hoffman 1988).

Strong shear wave splitting has been reported in the east-central US (Barruol *et al.* 1997; Fouch *et al.* 2000). Fouch *et al.* (2000) measured shear wave splitting at each station of the MOMA

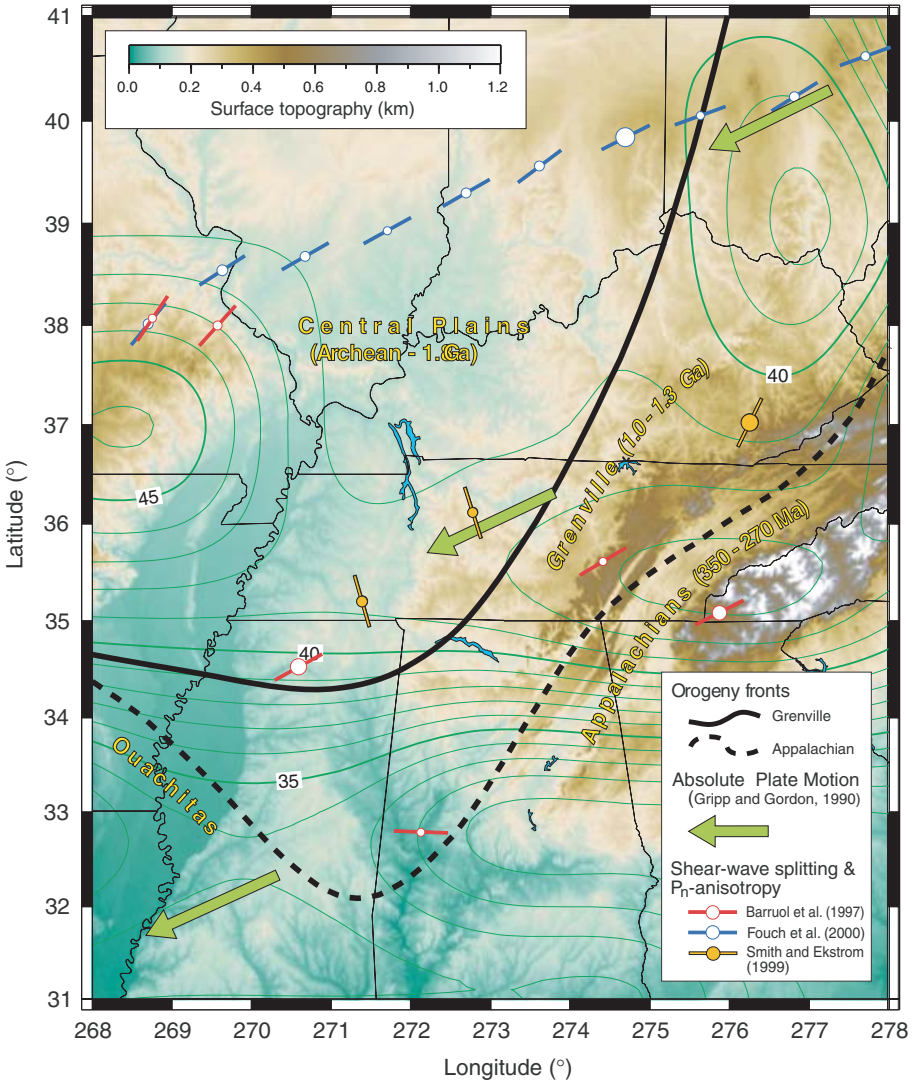

Figure 1. Tectonic setup. The background map shows surface topography from GTOPO30, and the dark green contour lines represent the Moho depth from crust2.0 (http://mahi.ucsd.edu/Gabi/rem.html) interpolated on a 0.2° × 0.2° grid mesh. The thick plain and dashed black curves denote the Grenville and Appalachian fronts, respectively. Also shown are the regional absolute plate motion (Gripp & Gordon 1990), shear wave splitting from Fouch *et al.* (2000) and Barruol *et al.* (1997), and P_n-anisotropy from Smith & Ekström (1999). Circle sizes are proportional to the amount of splitting.

network, and found splitting times between 0.5 and 2.2 s, depending on the station (Fig. 1, blue symbols). Barruol *et al.* (1997) compiled measurements in a wider region, and found similar directions of fast propagation, with more scatter (Fig. 1, red symbols). The directions of fast propagation fit well the regional absolute plate motion (Gripp *et al.* 1990) (Fig. 1, green arrows), supporting the hypothesis that shear wave splitting in this region results primarily from asthenospheric deformation due to the relative motion of the lithosphere and asthenosphere. However, due to the tectonic context, it is reasonable to assume that frozen fabric due to past deformation is also present in the lithosphere beneath the Appalachian and Grenville provinces, producing seismic anisotropy. This hypothesis is supported by P_n-anisotropy measurements (Smith & Ekström 1999), which shows different directions of fast propagation beneath the Central Plains and beneath the Grenville and Appalchian provinces (Fig. 1, orange symbols). Interestingly, the direction of fast propagation beneath the Grenville and Appalachian provinces is compatible with that inferred from shear wave splitting in this region.

Shear wave splitting measurements have an excellent lateral resolution, but poor radial resolutions and therefore cannot locate the anisotropy unambiguously. On the contrary, surface waves are sensitive to different depths depending on their period, and can thus constrain azimuthal anisotropy with a better radial resolution than shear wave splitting. Arrays are well suited to retrieve isotropic and anisotropic regional structures sampled by surface waves, but methodology and data availability often limit the explored period range (e.g. Friederich & Huang 1996; Freybourger *et al*. 2001; Li *et al*. 2003). Recently, dense arrays allowed the construction of high-resolution models of Rayleigh-wave phase velocity in various regions. For instance, Yang & Forsyth (2006) built a Rayleigh-wave phase velocity model for southern California in the period range 25–143 s, and retrieved regional average azimuthal anisotropy, which they attributed to both lithospheric deformation and asthenospheric flow, the latter locally disrupted by small-scale convection. Pedersen *et al.* (2006) measured Rayleigh wave dispersion curves for the Baltic Schield in a broad (15–190 s) period range, and

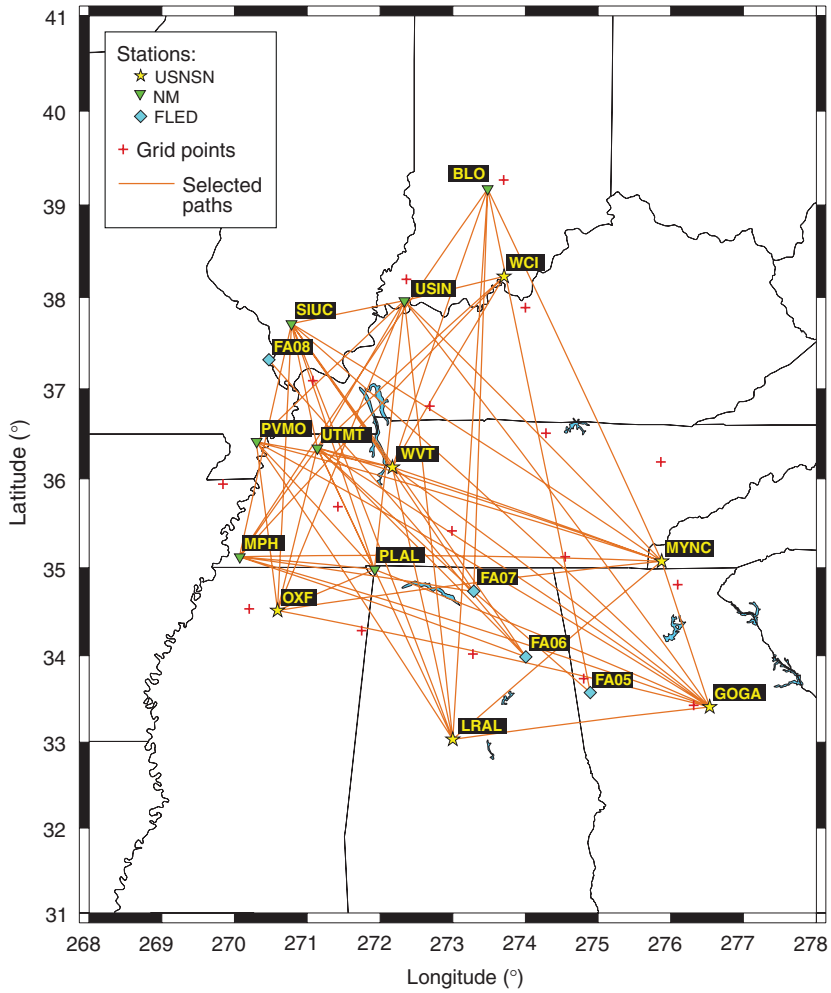

Figure 2. Data setup. Seismic stations are represented by different symbols, depending on the network they belong to. Selected paths used to compute the anisotropic model are shown in orange. The red crosses indicate the knots of the triangular grid on which the phase velocity model is calculated.

inferred azimuthal anisotropy in this region between 20 and 100 s. The amplitude of azimuthal anisotropy they observed was small between 20 and 60 s (sampling the lower crust and uppermost lithospheric mantle), but strongly increased in the period range 70–100 s (sampling the deep lithospheric mantle). Here, we measured dispersion curves of Rayleigh-wave phase velocity using a new implementation of the two-station method (Meier *et al.* 2004). Application of this technique to high-quality broad-band data enables measurements of interstations dispersion curves in a period range (10–200 s) that is broad enough to sample the Earth from the middle crust down to the subcratonic asthenosphere.

2 DATA AND REGIONAL SETTING

To investigate the Rayleigh-wave phase velocity structure of the east-central US (31°N–41°N, and 82°E–92°E), we used seismograms recorded at 17 seismic stations located in this area (Fig. 2). Most of these stations belong to permanent seismic networks (USNSN and NM), but we also used data from the Florida to Edmonton (FLED) temporary PASSCAL experiment (http://epsc.wustl.edu/seismology/FLED/proposal.html). Each pair of stations defines a path along which we can measure, data permitting, a phase–velocity dispersion curve for the fundamental Rayleigh mode.

The two-station method requires that the angles between the great circle connecting a pair of stations and the great circles connecting the stations and the event are not too large. In this study, we put this limit to 10°. Epicentral distances are between 10 and 170°, and all distances between pairs of seismic stations are smaller than 800 km. From the IRIS database, we extracted more than 20 000 records satisfying these criteria, from more than 3000 events. Events and source regions are different for each pair of stations. As an example, Fig. 3 shows event locations and great circles connecting events to the seismic stations for the pairs BLO-LRAL and MPH-MYNC. Due to global (distribution of source regions along the path azimuth) and local (site and instrumental qualities, station history) factors, the number of selected events greatly varies from one pair to another (Table 1). The interstation dispersion curve for a path connecting a pair of stations is averaged from all measurements for this pair of stations. Data availability and selection procedures resulted in the construction of average phase–velocity curves for 60 different paths (Fig. 2).

3 DISPERSION CURVES OF THE FUNDAMENTAL RAYLEIGH MODE

A collection of dispersion curves, one for each path connecting a pair of seismic stations of an array, can be used to constrain regional

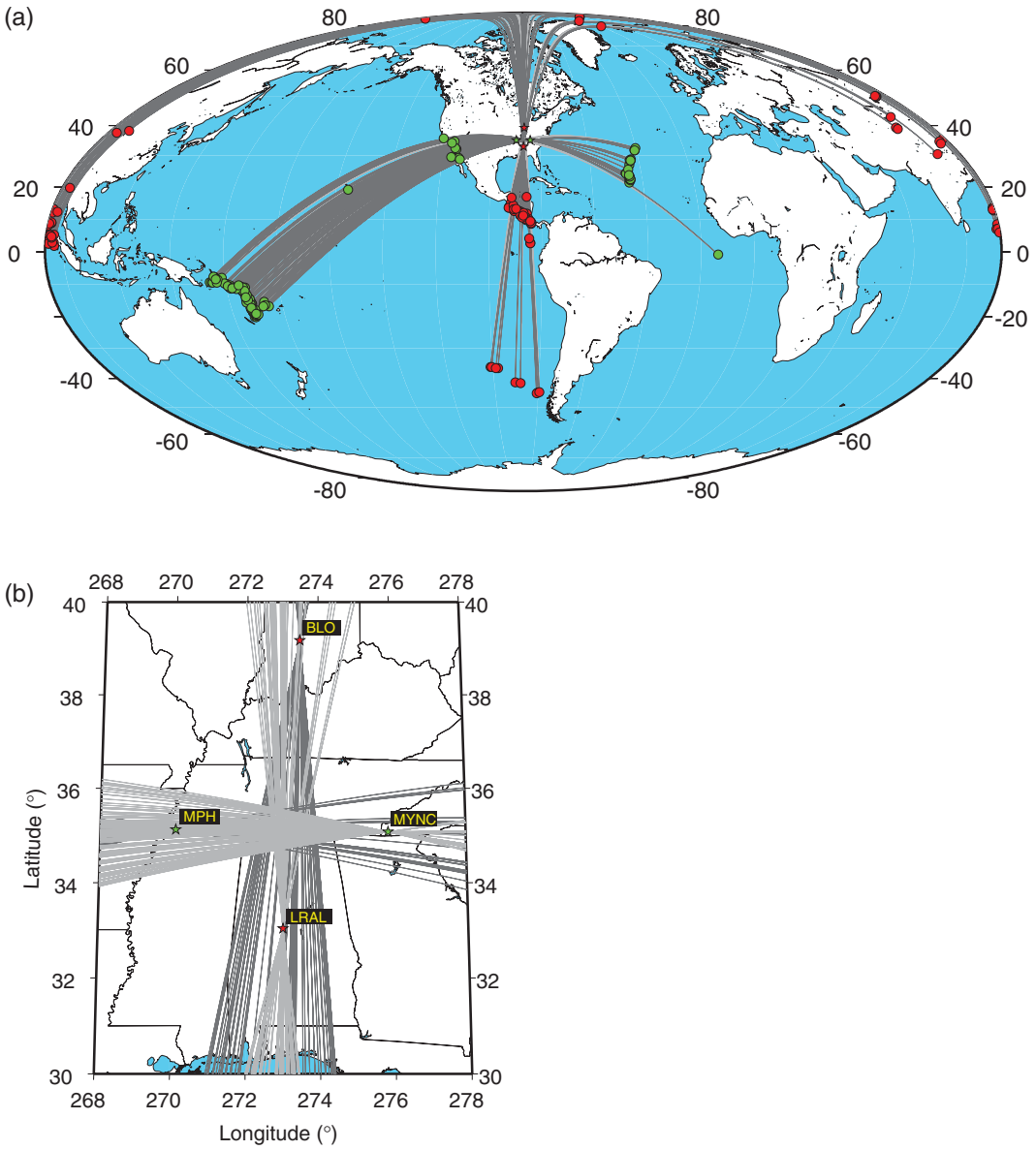

Figure 3. Events and great circles from events to stations for the pairs BLO-LRAL and MPH-MYNC. Red and green dots indicate the selected events for the pair BLO-LRAL and MPH-MYNC, respectively.

2-D variations in phase velocity beneath the array. The two-station method, first introduced by Sato (1955), has been extensively used to measure dispersion curves of surface waves (for a review of early works, see Knopoff 1972). In this study, we use a recent implementation of the cross-correlation approach (Meier *et al.* 2004). As shown below, this implementation allows measurements of dispersion curves in a broad period range (10–200 s).

For each selected event, the vertical components of the displacement recorded at the two stations of a pair are cross-correlated. To minimize the effects of noise and interferences, the cross-correlation function is first filtered with a frequency-dependent Gaussian band-pass filter. Side lobes caused by correlations of the fundamental mode with scattered waves or higher modes are then down weighted by applying in the time domain a frequency-dependent Gaussian window to the filtered cross-correlation function. This approach to filtering and windowing is effective as long as the fundamental mode has the largest amplitude on the seismogram and, consequently, on the cross-correlation function. The cross-correlation is then transferred in the frequency domain, and its complex phase $\Phi(\omega)$ is used to calculate the phase velocity $c(\omega)$ following

$$c(\omega) = \frac{\omega\,(\Delta_1 - \Delta_2)}{\zeta(\omega)}, \quad \zeta(\omega) = \arctan\left\{\frac{\mathrm{Im}\,[\Phi(\omega)]}{\mathrm{Re}\,[\Phi(\omega)]}\right\} + 2n\pi, \quad (1)$$

where Δ_1 and Δ_2 are the epicentral distances to each of the two stations. Because of the 2π ambiguity of the *arctan* function, the solution of eq. (1) is non-unique and is represented by an array of curves (one for each $n \in N$). Phase velocity is measured within a frequency range that is chosen interactively. Several non-overlapping frequency ranges can be selected for one single event. Seismic-wave diffraction and interference of Rayleigh- and Love-wave, fundamental and higher modes can bias the measurements. These effects, however, have a strong frequency dependence, which manifests itself in irregularities and roughness of measured curves. Selection of only smooth portions of the curves, removal of outliers

Table 1. Selected pairs.

Pair	D (km)	Az (°)	N_{eve}	N_t	f (mHz)	σ_C (m s^{-1})
BLO-FA05	634.1	−11.1	77	51	7.0–79.5	26.8
BLO-FA07	493.1	1.9	31	18	12.0–89.0	25.5
BLO-LRAL	682.3	3.5	67	43	4.5–77.5	36.5
BLO-MPH	541.8	33.0	153	85	5.0–100.0	31.6
BLO-MYNC	285.5	−24.4	123	43	4.0–110.4	31.2
BLO-WVT	356.8	18.5	72	33	7.5–129.4	30.5
FA05-FA07	195.7	−48.5	50	13	17.5–132.9	33.5
FA06-FA08	489.0	−39.9	16	10	24.5–79.5	16.1
GOGA-LRAL	331.8	81.8	65	37	4.0–101.5	33.1
GOGA-MYNC	194.2	−18.1	171	50	5.0–119.4	25.0
GOGA-OXF	562.6	−75.8	110	48	4.5–94.0	29.6
GOGA-WVT	500.4	−51.7	110	34	3.5–110.4	36.1
LRAL-MYNC	348.3	48.7	32	32	7.0–122.4	30.4
LRAL-WVT	351.7	−12.3	73	58	3.0–79.5	34.4
MPH-FA06	383.0	−69.6	22	14	25.5–89.0	27.5
MPH-FA07	297.5	−80.7	31	20	16.5–94.0	27.6
MPH-GOGA	624.8	−70.5	117	80	3.0–81.5	33.9
MPH-MYNC	529.2	88.9	39	24	4.5–96.5	28.3
MPH-PLAL	170.1	−84.2	130	113	5.0–81.5	31.5
MPH-SIUC	294.6	12.4	145	86	5.5–126.0	28.5
MPH-UTMT	166.2	35.2	103	65	6.5–129.4	29.6
MPH-WCI	473.8	42.3	47	40	14.5–110.4	26.9
MYNC-OXF	487.3	81.2	91	32	16.5–96.5	30.5
MYNC-WVT	355.3	−69.7	68	30	5.0–126.0	38.9
PLAL-GOGA	459.1	−66.4	98	63	5.0–110.4	41.8
PLAL-OXF	132.8	66.5	89	13	15.0–69.5	46.5
PLAL-PVMO	216.4	−42.3	101	31	21.5–116.4	25.6
PLAL-SIUC	320.1	−18.3	203	41	3.0–91.5	53.8
PLAL-USIN	333.0	6.2	24	27	15.0–107.4	20.6
PLAL-UTMT	166.9	−25.1	172	22	5.0–96.5	27.2
PVMO-GOGA	659.6	−57.9	36	22	7.0–79.5	24.0
PVMO-LRAL	449.1	−32.7	127	68	6.0–119.4	26.4
PVMO-MYNC	525.4	−72.0	34	12	9.0–89.0	27.2
PVMO-OXF	212.7	−7.0	81	17	7.5–67.5	24.3
PVMO-USIN	249.5	45.8	44	37	14.0–132.9	20.9
PVMO-WVT	170.9	−78.8	45	18	7.0–77.5	29.9
SIUC-FA06	506.0	−34.2	37	29	5.5–104.5	25.3
SIUC-FA07	400.5	−33.5	48	31	8.5–77.5	30.2
SIUC-GOGA	706.7	−45.9	157	73	3.5–77.5	34.3
SIUC-LRAL	557.0	−20.6	92	43	4.0–96.5	31.3
SIUC-MYNC	542.4	−55.8	69	26	8.0–94.0	28.6
SIUC-OXF	355.8	2.7	98	25	3.5–107.4	26.8
SIUC-USIN	139.4	78.0	108	30	6.5–58.5	37.2
SIUC-UTMT	155.5	−11.6	235	15	19.5–63.5	26.5
SIUC-WVT	215.0	−34.7	171	61	5.0–143.4	36.3
USIN-GOGA	632.1	−35.8	98	45	4.0–84.0	21.9
USIN-LRAL	550.3	−6.1	94	49	4.5–75.5	31.7
USIN-MYNC	450.9	−43.6	89	32	7.0–119.4	29.6
USIN-OXF	414.0	21.7	43	16	20.0–107.4	20.3
USIN-UTMT	209.2	30.2	55	22	18.5–99.0	26.8
USIN-WCI	123.8	75.9	91	44	24.5–163.4	46.3
UTMT-FA06	369.9	−44.2	29	15	27.5–89.0	23.8
UTMT-FA07	264.7	−46.9	36	15	28.5–84.0	25.1
UTMT-GOGA	590.8	−55.1	98	40	5.0–94.0	31.8
UTMT-LRAL	404.8	−24.5	94	31	5.0–96.5	30.4
UTMT-MYNC	451.1	−70.5	65	31	15.0–96.5	27.6
UTMT-OXF	209.0	13.5	75	10	20.0–126.0	27.6
UTMT-WCI	309.5	47.6	53	37	17.5–155.4	27.5
WCI-WVT	269.9	29.9	81	24	18.0–126.0	34.1
WVT-UTMT	95.9	−75.5	68	23	22.5–75.5	31.3

Note: For each pair, we list the distance between the two stations (D), the azimuth of the path (Az), the number of event downloaded from the IRIS database (N_{eve}), the number of events used to build the phase velocity dispersion curve (N_t), the frequency range of the dispersion curve (f), and the estimated average standard deviation in phase velocity (σ_C).

(unrealistically far from the reference), and subsequent averaging over many measurements strongly minimize these effects and turn out to be sufficient to warrant the accuracy of the measured dispersion in almost all cases (Meier *et al.* 2004; Lebedev *et al.* 2006; Pedersen 2006). Remaining biases are substantial only in areas of exceptionally strong lateral heterogeneity. Even in these cases, however, the biases are usually easy to identify by inconsistency from measurements on waves arriving from different source regions, especially from the opposite directions.

The selection of the frequency ranges is thus based on the smoothness of the dispersion curves and on the consistency between these curves and an initial *a priori* dispersion curve. Further information for the selection of frequency range(s) is given by time–frequency plots of the two seismograms and of the cross-correlation function, illustrating the properties of the waveforms of the fundamental Rayleigh mode (Meier *et al.* 2004). Scattering and noise are easily detected on these plots. The operations described are performed on the records of all selected events, leading to a collection of phase velocity measurements in various frequency ranges (Figs 4a–d). Selected measurements for a given pair of stations are then assembled to compute averages and standard deviations of the phase velocity along the path that connects the two stations. This averaging reduces biases due to seismic-wave diffraction and interferences between the fundamental and higher modes.

We constructed dispersion curves for 60 different paths (Fig. 2, orange lines). Depending on the number and characteristics of available seismograms, the accuracy of the dispersion curves and the frequency range in which they were measured vary from path to path. For instance, the dispersion curve for path MPH-FA07 (Figs 4d and h) was constructed with 20 events, but poor quality of the data did not allow estimates of the velocity outside the frequency range 16.5–94 mHz (period range 11–60 s). For most paths, however, data allowed the determination of phase velocity between 10 and 80 mHz (100 and 12 s) with a standard deviation around 30 m s^{-1} (Table 1). All 60 paths cover the frequency range 30–55 mHz (period range 18–34 s). For many paths (33) the dispersion curve extends down to a frequency of 7 mHz (up to a period of 140 s), and for about 1/3 of the paths (e.g. GOGA-USIN, Figs 4a and e, and OXF-SIUC, Figs 4c and g), we could measure the dispersion curve down to a frequency of 5 mHz (up to a period of 200 s). The regional coverage also varies with period (Fig. 5). The path density is slightly higher in the western half than in the eastern half at all periods, but on the whole the selected paths fully cover the explored area, even at $T = 10$ s where only 27 paths are available. The azimuthal repartition of paths (histograms in Fig. 5) shows a slight excess of paths with azimuth between $-90°$ and $0°$ (in particular around $\Psi = -40°$).

Our collection of dispersion curves thus covers a broad period range and yields a dense coverage of the explored area for periods between 12 and 140 s. Given the sensitivities of Rayleigh waves (Fig. 6), we can expect our dispersion curves to constrain the seismic structure of both the lower crust and the upper half of the upper mantle. A qualitative comparison between the phase velocity curves for each path and the regionally averaged phase velocity curve (dashed red curves in Figs 4e–h) reveal substantial variations in the phase velocity. These anomalies may be both isotropic and anisotropic in origin.

Although our dispersion curves are each averaged from many measurements and are overall smooth, a certain roughness of small scale and small amplitude is still present. To test whether this small-scale roughness has some effect on the phase velocity maps, we computed the maps both using the original curves and using the curves that were smoothed further. This additional smoothing was

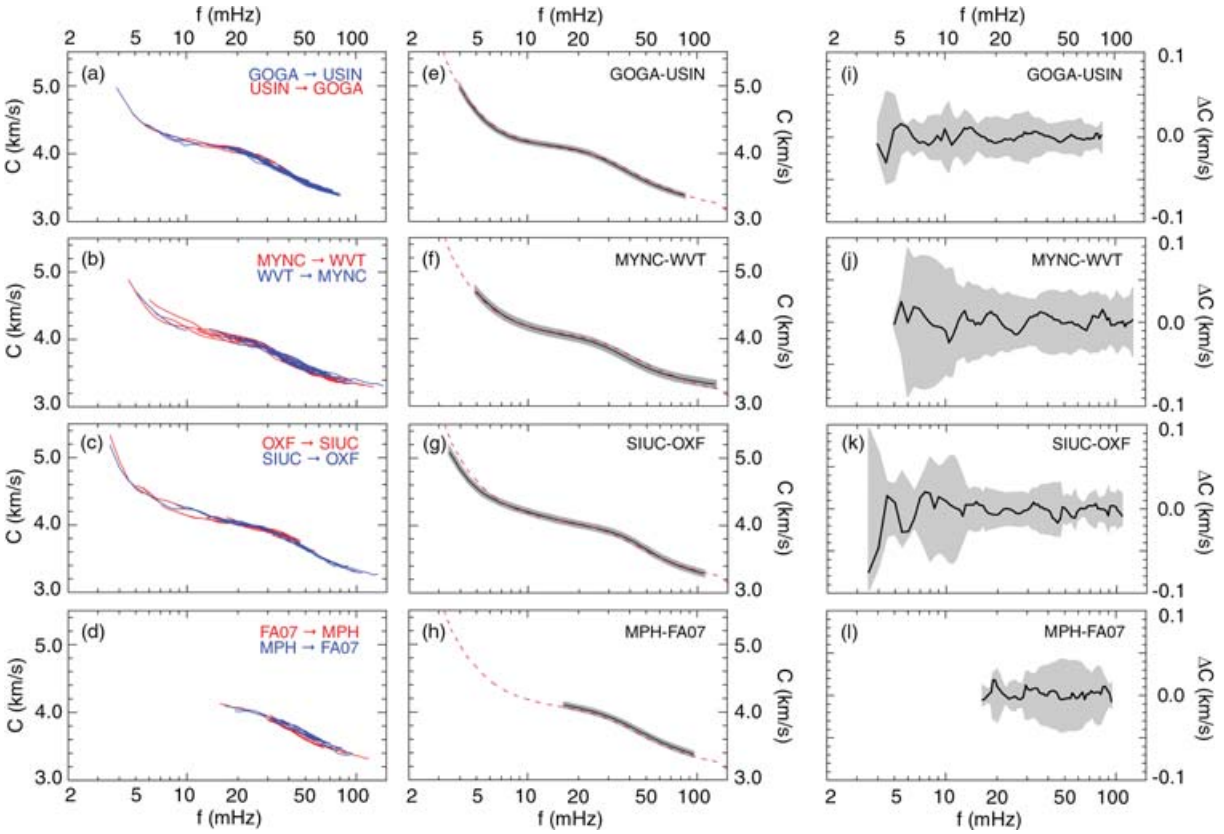

Figure 4. Phase velocity dispersion curves for four different paths. Panels (a–d) plot measurements used to construct the average curves. The direction of propagation is indicated by the colour code (red or blue). In panels (e–h), the bold black lines represent the average smoothed dispersion curves, and the shaded areas cover one standard deviation around this average. The red dashed curve in each plot shows the phase velocity curve averaged over all the 60 paths. Panels (i–l) show the differences between the original and smoothed average dispersion curve.

performed by means of inverting each dispersion curve for a radial model of shear wave velocity (as in Section 5). The inversion is regularized very weakly. It produces a (not necessarily realistic) radial model from which we calculate a theoretical phase velocity curve that is taken as the smoothed version of the original curve. It is important to note that the smoothed dispersion curves fit well within the observed standard deviations and are very similar to the observed average dispersion curve (Figs 4i–l). This approach is in line with the realization that a path-average V_S profile can be seen as a summary of the dispersion properties of the medium along a path for one ore more surface wave modes (Yoshizawa & Kennett 2002; Visser *et al.* 2007). When we inverted the phase–velocity curves with and without the additional smoothing, we found that the differences in the resulting phase–velocity maps were minimal. In the following we use the smoothed curves but acknowledge that the smoothing has not produced any appreciable effect. This could be expected given that the differences between the smoothed and original curves are small and well within the error bars.

The standard deviation in the measured phase velocity at each period is a good estimate of the error in the dispersion curve. The error generally increases with period. In this study, we compute phase–velocity maps by inversions of dispersion curves at different periods that are set up independently from each other (Section 4), rather than by inverting single-path dispersion curves for path-averaged V_S profiles. The phase velocity maps will be thus affected by variations in the errors from one path to another, rather than by the frequency dependence of the errors. For this reason, we chose to use a frequency-independent estimated error for every dispersion curve and fixed the value of this error to the rms of the observed error over the frequency range of the curve.

4 REGIONAL ANISOTROPIC PHASE VELOCITY MAPS

To separate isotropic and anisotropic contributions to the Rayleigh-wave phase velocity anomalies, we performed simultaneous inversions for regional variations in these contributions at each period. The anisotropic part is described by a 2Ψ and a 4Ψ contribution (Smith & Dahlen 1973). Previous studies (Montagner & Tanimoto 1991; Trampert & Woodhouse 2003) showed that 4Ψ-anisotropy is not negligible and should be accounted for in the inversion. The total phase velocity anomaly at longitude φ and latitude θ is given by

$$\delta C(\varphi,\theta) = \delta C_{iso}(\varphi,\theta) + \delta C_{2\Psi}(\varphi,\theta) + \delta C_{4\Psi}(\varphi,\theta), \quad (2)$$

where $\delta C_{\rm iso}$ is the isotropic anomaly, and $\delta C_{2\Psi}$ and $\delta C_{4\Psi}$ are the 2Ψ- and 4Ψ-anisotropic anomalies defined by

$$\delta C_{2\Psi}(\varphi,\theta) = A_{2\Psi}\cos(2\Psi) + B_{2\Psi}\sin(2\Psi), \quad (3a)$$

$$\delta C_{4\Psi}(\varphi,\theta) = A_{4\Psi}\cos(4\Psi) + B_{4\Psi}\sin(4\Psi), \quad (3b)$$

respectively, where Ψ is the local azimuth of the ray, and $A_{2\Psi}$, $B_{2\Psi}$, $A_{4\Psi}$ and $B_{4\Psi}$ are four anisotropic coefficients defined for each longitude φ and latitude θ. The amplitudes of anisotropic anomalies,

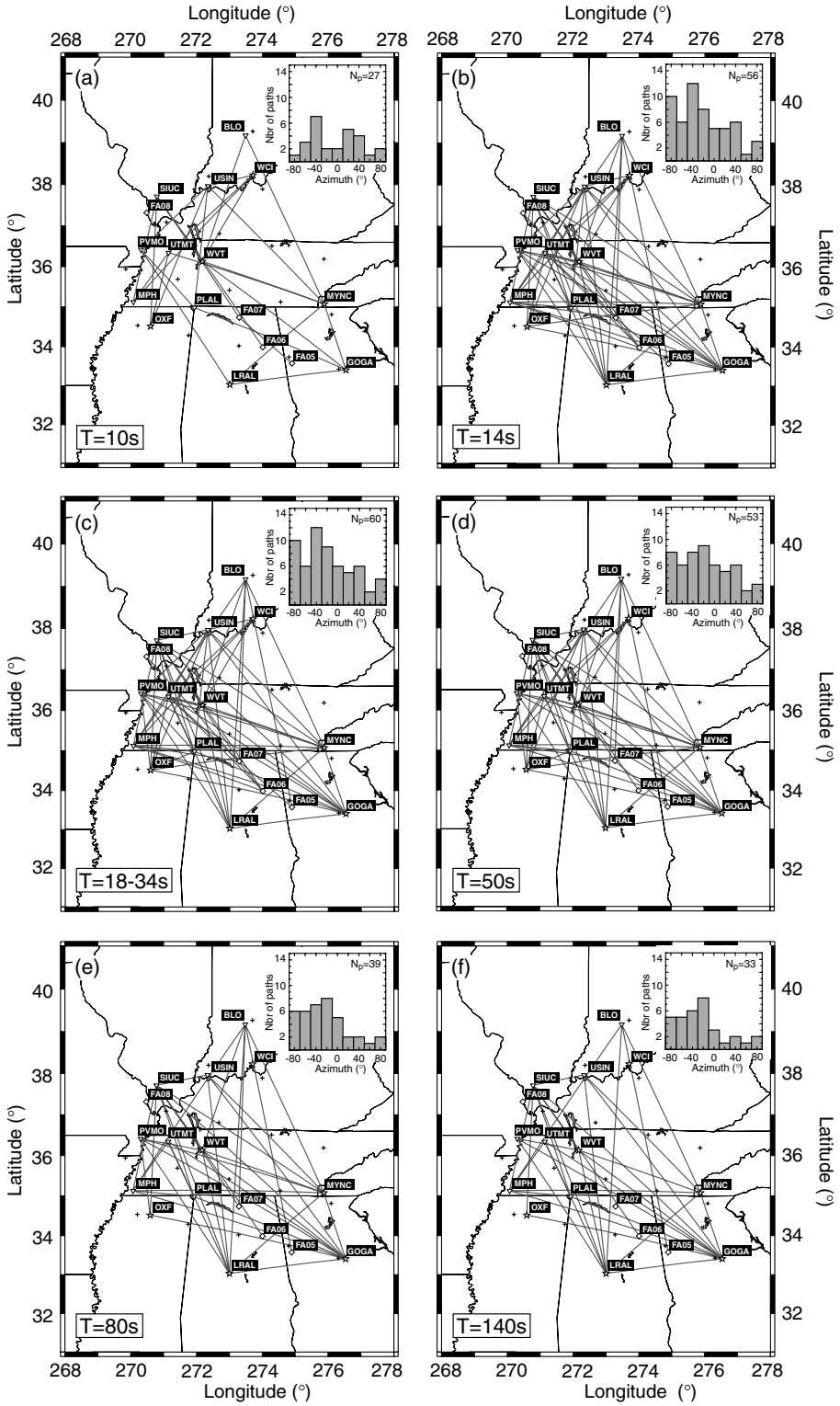

Figure 5. Path coverage at six periods. For each period (or period range) the N_p selected paths are shown in dark grey, and the azimuthal distribution of the selected paths is plotted in a histogram.

Λ, and the directions of fast propagation, Θ, are given by

$$\begin{cases} \Lambda_{2\Psi} = \sqrt{A_{2\Psi}^2 + B_{2\Psi}^2} \\ \Theta_{2\Psi} = \frac{1}{2}\arctan\left(\frac{B_{2\Psi}}{A_{2\Psi}}\right) \end{cases} \quad \text{and} \quad \begin{cases} \Lambda_{4\Psi} = \sqrt{A_{4\Psi}^2 + B_{4\Psi}^2} \\ \Theta_{4\Psi} = \frac{1}{4}\arctan\left(\frac{B_{4\Psi}}{A_{4\Psi}}\right) \end{cases}. \quad (4)$$

We thus invert our collection of phase velocity dispersion curves for five parameters, $\delta C_{\rm iso}$ and the four anisotropic coefficients.

The model is parametrized on a triangular grid (Wang & Dahlen 1995) of 32 knots with a grid spacing of 140 km. In post-processing (inversion for radial models of V_S), we did not account for the

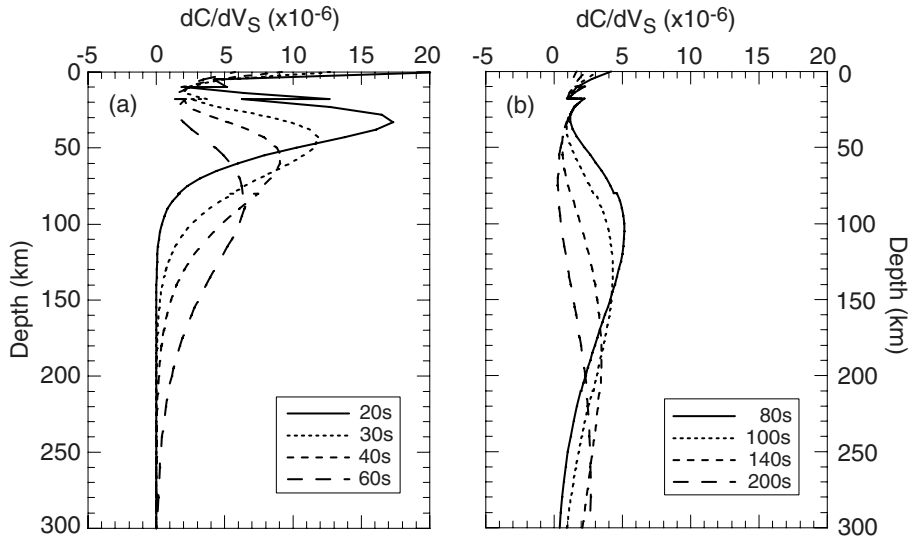

Figure 6. Depth sensitivity kernels of Rayleigh waves for periods between 20 and 200 s. The Frechet derivatives are for isotropic terms, but they can also give an idea of the radial distribution of the azimuthal anisotropy (Montagner & Nataf 1986).

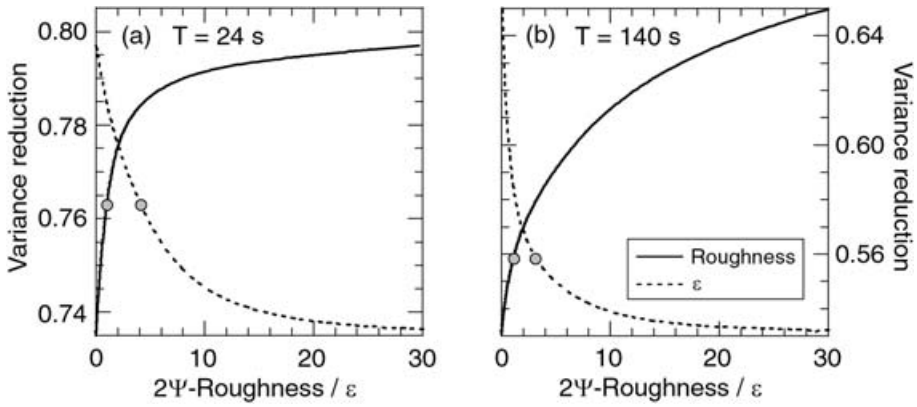

Figure 7. Trade-off curves. The variance reduction is plotted and as a function of the smoothness coefficient ε (dotted curves) and of the roughness in the distribution of 2Ψ-anisotropy anomalies (plain curves). Smoothness coefficients for isotropic anomalies and 4Ψ-anisotropic terms are kept constant. The circles indicate our preferred model. (a) $T = 24$ s; preferred model is for $\varepsilon = 4.2$. (b) $T = 140$ s; preferred model is for $\varepsilon = 3.1$.

peripheral knots, where resolution is poorer, and kept only 17 knots (red crosses in Fig. 2). At each period, the average phase–velocity anomaly along the path i is

$$\overline{\delta C_i} = \int_\varphi \int_\theta K_i(\varphi, \theta)\, \delta C(\varphi, \theta)\, \mathrm{d}\theta\, \mathrm{d}\varphi, \tag{5}$$

where the local anomalies $\delta C(\varphi,\theta)$ are given by eqs (2) and (3). The sensitivity kernels $K_i(\varphi,\theta)$ contain the weight of each knot for that particular path (Lebedev & van der Hilst 2006), and were approximated by paths of finite width. In the calculations, we fixed the path width to 20 km. We varied the path width between 10 and 300 km, but did not find significant differences in the results. The rms of the discrepancies between solutions obtained with different values of the path width is about 2 m s^{-1}, that is, much less than the rms of the estimated error bar on isotropic and anisotropic parameters, which is around 8–12 m s^{-1}. This result suggests that the effect of the assumption of the width of the sensitivity area is limited. For each period, we build a system of linear equations (one equation for each available path at the period, i.e. maximum 60) based on a discrete version of eq. (5) (see Appendix). We then solve this system using the LSQR method (Paige & Saunders 1982) with lateral smoothing and slight norm damping. Isotropic and anisotropic terms are smoothed and damped independently. Choosing the amount of smoothing and damping is always subjective. We defined our preferred model as a compromise between model smoothness and ability to explain observed data (variance reduction). Compromise can be visualized on trade-off curves, as those plotted in Fig. 7. The smoothing we imposed penalizes the second spatial derivatives of each term. Strong smoothing will therefore result in a constant gradient in the inferred distribution.

Estimates of uncertainties due to measurement errors

LSQR does not provide covariances matrices. In order to estimate error bars in the model parameters due to measurement errors, we perform a Monte Carlo search. At each period, we randomly perturb the dispersion curves within their uncertainties. The random noise is generated from a Gaussian probability distribution with a zero mean and standard deviations equal to the curve uncertainties. We then invert this set of perturbed dispersion curves for a perturbed regional model of phase velocity (including isotropic and anisotropic anomalies). By repeating these operations a large number of times

(100 000), we obtain a set of phase velocity models, from which we compute the average anomalies (isotropic and anisotropic) and their standard deviations. These standard deviations are good estimates of the uncertainties in dispersion measurements. The regional rms of these uncertainties vary between 8 and 12 m s^{-1}, depending on the period and the parameter considered.

Importance of anisotropy

To test the significance of anisotropy in explaining our data, we first performed an inversion in which anisotropic terms are neglected. Damping and smoothing are similar to those of the preferred model. Because the number of inverted parameters is not the same, comparing the variance reductions obtained in each inversion is meaningless. Instead, we computed the reduced χ^2 defined as (Trampert & Woodhouse 2003)

$$\chi^2 = \frac{1}{(N_p - T)}(\mathbf{d} - \mathbf{Gm})^{\mathbf{T}}\mathbf{C}_{\mathbf{d}}^{-1}(\mathbf{d} - \mathbf{Gm}), \quad (6)$$

where N_p is the number of data, T the trace of the resolution matrix, **d** and **m** the data and model vectors, **G** the kernel matrix (eq. A3) and $\mathbf{C_d}$ the covariance matrix. Fig. 8 plots the resulting χ^2 as a function of period. Models with lower reduced χ^2 explain the data better. To decide whether differences in reduced χ^2 are significant, we performed F-tests (Bevington & Robinson 1992). For all periods, the reduced χ^2 is smaller when anisotropy is accounted for (Fig. 8). This difference is the largest in the period ranges 16–34 s and 120–160 s, and F-tests show that these differences are 99 per cent significant. Between 36 and 80 s, the decrease in χ^2 is modest, and F-tests indicate that it is only 36 per cent significant. Note that at periods greater than 160 s, the reduced χ^2 is large even when anisotropy is accounted for. In this period range, our results may be less reliable due to poorer data and azimuthal coverage. The reduced χ^2 decrease further when 4Ψ terms are accounted for, but compared to the model with isotropic and 2Ψ terms only, differences are very small and F-tests show that they are not significant. These tests demonstrate that azimuthal 2Ψ-anisotropy is needed to explain the data in period ranges 16–34 s, 120–160 s.

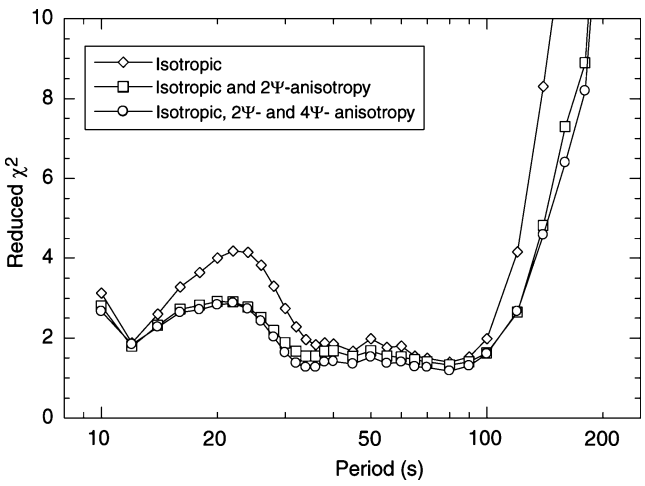

Figure 8. Reduced χ^2 as a function of period. Inversion is performed for isotropic anomalies only (diamonds), isotropic and 2Ψ-anisotropy anomalies (squares), and isotropic and full anisotropy (2Ψ and 4Ψ) (circles). The damping and smoothing factor are those of the preferred model.

Preferred model

The isotropic and anisotropic anomalies of our preferred model are displayed in Fig. 9 for various periods. Throughout this paper, isotropic and anisotropic anomalies are relative to a reference model that is defined as the regional average of the isotropic dispersion curve (Fig. 10c). The regional rms amplitudes of the relative isotropic, and 2Ψ-anisotropic anomalies are shown in Fig. 10. The 4Ψ-anisotropic terms are not needed to explain the data (see previous subsection), and in the remainder of the paper we will focus on isotropic and 2Ψ-term (hereafter simply referred to as anisotropy) anomalies.

Isotropic phase–velocity anomalies

The distribution and average amplitude of isotropic anomalies strongly depends on the period. Largest anomalies are found in the period range 16–34 s. At 20 s, for instance, the average amplitude is ∼0.8 per cent of the reference velocity, but the maximum amplitude is close to 1.7 per cent. Between 40 and 140 s, deviations from the regional average are small, 0.3 per cent on average. At longer periods (160 s and above), amplitudes of anomalies increase again, and are comparable to those observed between 16 and 32 s.

The dominant feature in the distribution of isotropic anomalies is a negative velocity gradient from SW to NE in the period range 12–50 s. This gradient is strongest between 16 and 32 s. There are some indications for the persistence of the SW–NE gradient up to 60 s, but on the whole, between 55 and 100 s, fast anomalies are confined to the SW portion. Finally, at periods larger than 120 s, we observe a pocket of fast anomalies that increases in amplitude with increasing period.

Anisotropic phase–velocity anomalies

We observe strong anisotropy between 20 and 34 s, with significant regional variations in the amplitude and azimuth of the fast-propagation direction. Beneath the orogenic terrains (Grenville and Appalachian), the average amplitude reaches 1 per cent of the reference velocity, and the azimuth of the fast-propagation direction is regionally uniform. West of the Grenville front, the average amplitude is smaller (∼0.5 per cent), and the fast-propagation directions are less uniform. Between 45 and 60 s, in contrast, azimuthal anisotropy is weaker, reaching only ∼0.5 per cent in amplitude. The direction of fast propagation is laterally uniform and equal to 165°, that is, nearly perpendicular to the fast-propagation direction observed in the range 20–34 s. We do not see indications for strong azimuthal anisotropy in the period range 65–100 s. The average amplitude is small (<0.4 per cent), and the azimuth of fast-propagation direction is not regionally uniform. Around 140 s, we observe substantial anisotropy again. The amplitude of anisotropy is large, >1 per cent on average, and the azimuth of fast-propagation direction is regionally uniform around 54°. At 160 s, the average amplitude and the azimuth of fast-propagation direction are comparable to those at 140 s, but there is more variability in the azimuths. Finally, at 180 s and longer periods (not shown), the amplitude of anisotropy is large, but the azimuth of the fast-propagation direction is not regionally coherent. Only 23 paths could be used at these long periods (compared to 60 for periods between 20 and 34 s, and 33 around 140 s), and most of them have an azimuth between −90° and 0°, which probably biases the model.

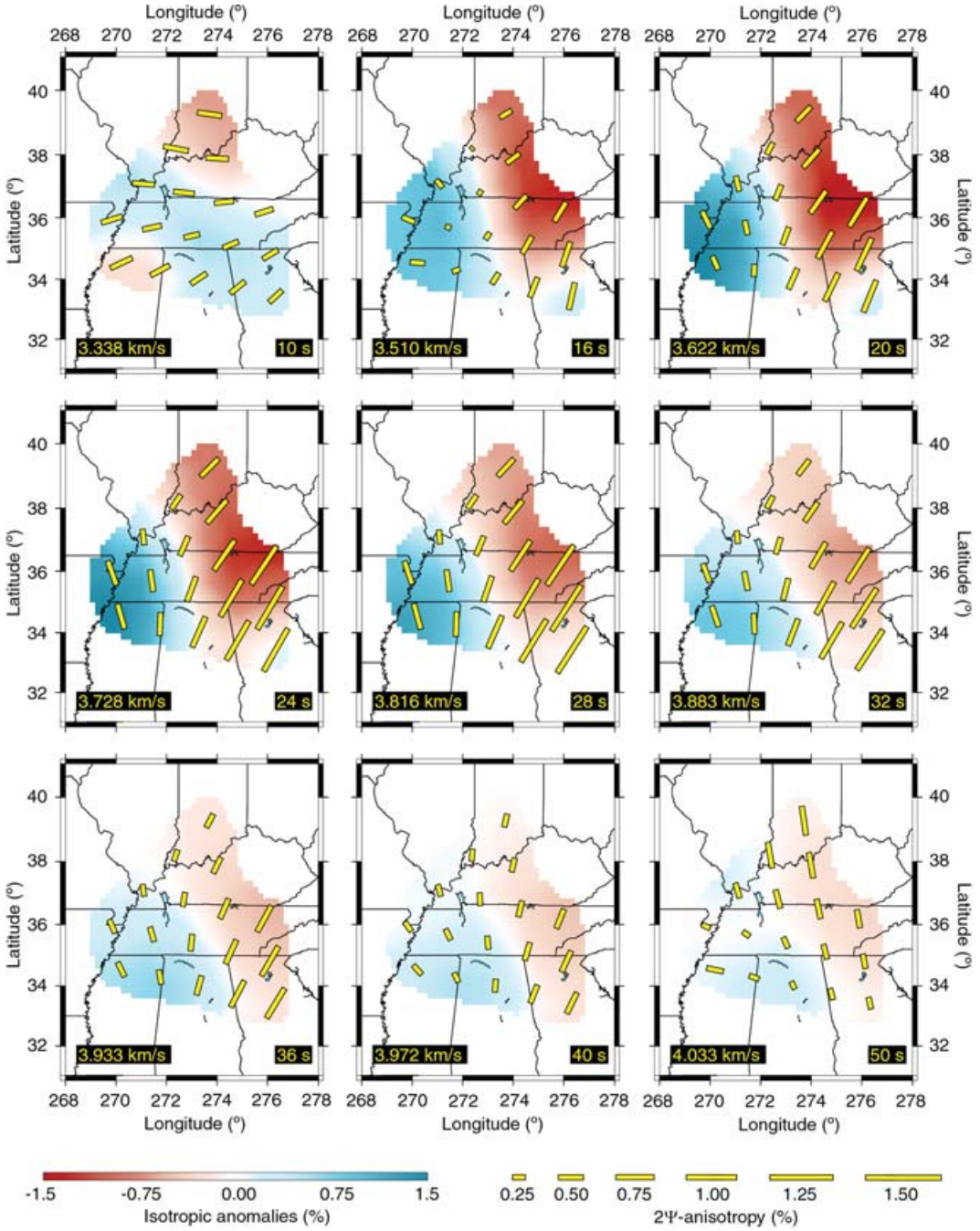

Figure 9. Relative isotropic and anisotropic anomalies of our preferred model at various periods. The length and the direction of the bars denote the amplitude and the fast-propagation direction of anisotropy, respectively. All anomalies are relative to the regional average dispersion curve (Fig. 10c). The value of the reference velocity at each frequency is indicated on each plot.

Influence of regularization

The type and strength of smoothing influence the results of the inversions. The smoothing we imposed penalizes the second lateral derivatives of the phase velocity distribution, and is therefore well suited to retrieve regular gradients in seismic anomalies. Large-scale gradients in phase velocity anomalies will be recovered by our inversions, whereas small local anomalies, if present, will be averaged out by smoothing and will not appear in our models.

The choice of the amount of smoothing is subjective. To estimate the influence of the smoothing coefficient ε on the models, we both plotted trade-off curves (Fig. 7) and examined the results of inversions with different values of the smoothing coefficients. Fig. 11 shows the influence of the smoothing of anisotropy at 24 s. There are large discrepancies between the anisotropic patterns obtained with small smoothing coefficients ($\varepsilon = 2.5$ and less), but interestingly, the azimuths of fast-propagation direction obtained with values of ε larger than 3.0 are not very sensitive to ε. The influence of smoothing

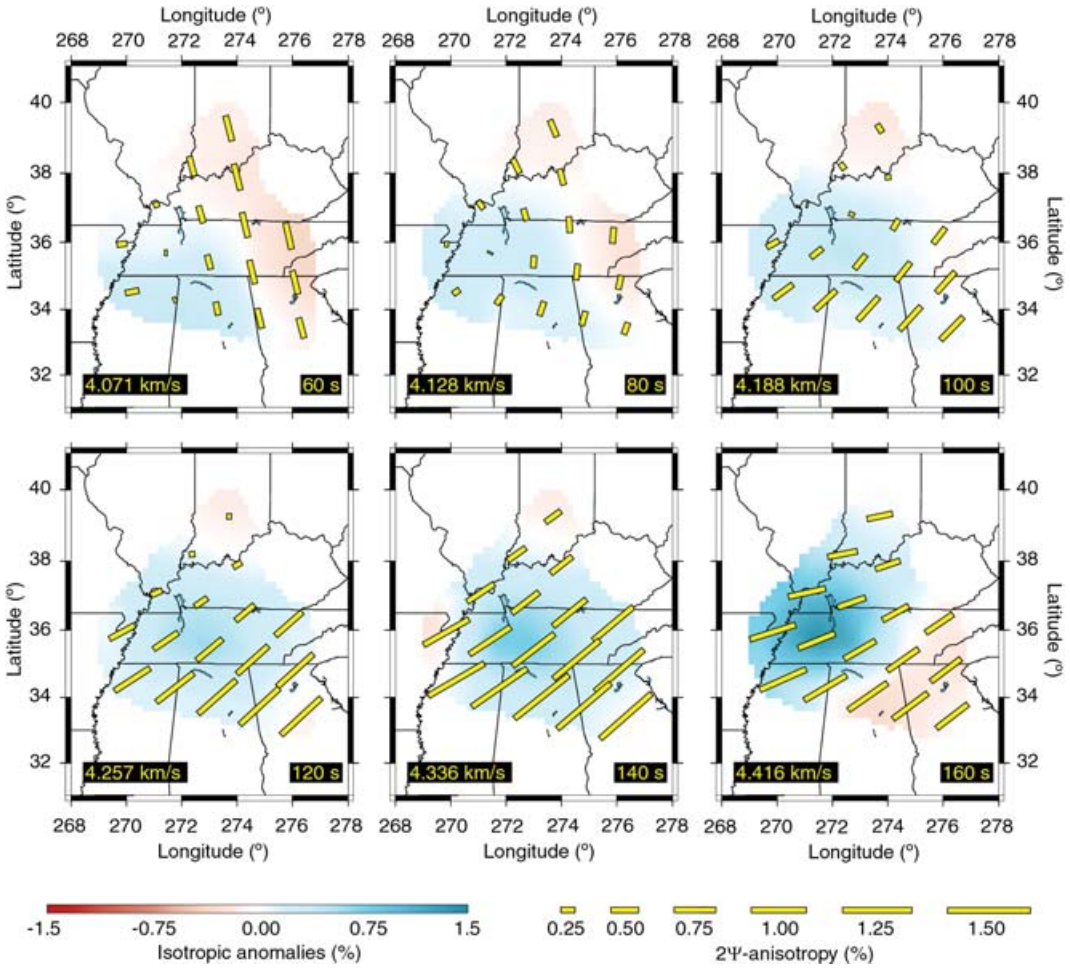

Figure 9. (*Continued.*)

on the amplitude of anisotropy is stronger. The rms of the amplitude of anisotropy at 24 s with $\varepsilon = 3$ and 10 are equal to 0.8 and 0.5 per cent, respectively.

Data sampling varies with the period. All 60 paths sample the period range 18–34 s, but periods outside this range are more sparsely sampled (for instance, only 20 paths sample periods up to 200 s). If we use the same damping coefficients with our damping scheme at all periods, the maps at period with weak sampling will be oversmoothed. To avoid such oversmoothing, we have adjusted the damping coefficient with period.

Trade-off and resolution matrices

To estimate the trade-off between isotropic and anisotropic terms, we defined test models m^{test} in which the isotropic anomalies are equal to those of the preferred model, and the anisotropic anomalies have been set to zero. We then compute test data

$$d^{\text{test}} = Gm^{\text{test}}, \tag{7}$$

and invert them for phase velocity anomalies (Fig. 12). Damping and smoothing coefficients are similar to those used for the preferred model. Clearly, the isotropic anomalies are very close to those of our preferred model. Between 20 and 40 s, there are small discrepancies in the structure (for instance, the southeast corner at 24 s is now slower than average), but the regionally average amplitudes are 80 per cent of that observed in our preferred model. At longer periods, the amplitude discrepancy slightly increases. More importantly, the amplitudes of artificial 2Ψ-term anisotropy are very small, about 2 m s^{-1} on average, at all periods. This series of inversions suggest that trade-off between isotropic and anisotropic terms do exist, but are small.

The LSQR method does not directly provide resolution matrices. It is possible, however, to reconstruct the resolution matrix **R** by 'inverting' each column j of the kernel matrix **G** (Trampert & Lévêque 1990). Given the LSQR operator, **L**, we have

$$R = LG \tag{8}$$

and, therefore, for each column j,

$$R_j = LG_j. \tag{9}$$

Fig. 13 shows resolution matrices at 24 and 140 s. If the inverted parameters are perfectly resolved, the resolution matrix is equal to the identity matrix, whereas smearing indicates linear dependencies between inverted parameters. Fig. 13 confirms that trade-offs between isotropic and anisotropic terms are present, but limited. In the diagonal submatrices, stronger lateral (or geographical) trade-offs in the distribution of each of the isotropic and anisotropic terms are apparent. These geographical trade-offs are mostly due to the imposed smoothness.

The effect of smoothing is to spread out local anomalies. As a consequence, narrow anomalies of the same sign can be distinguished

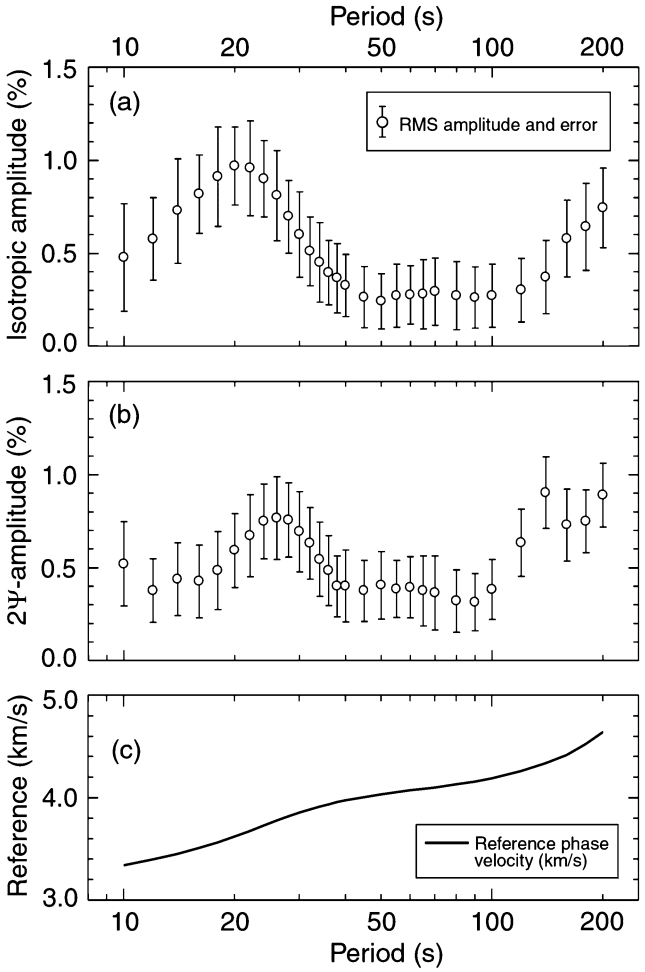

Figure 10. The rms amplitude and error of relative isotropic anomalies (a) and 2Ψ-anisotropy anomalies (b) as a function of period. Errors are due to the uncertainties in the dispersion curves. (c) Regional average isotropic dispersion curve.

only if they are distant enough. The shortest distance at which they can be resolved is the resolution length, also equal to the half width of the image of a δ-function anomaly as it would appears in the model (Lebedev & Nolet 2003). Note that anomalies wider than the resolution length and sharp transitions with anomaly sign change are correctly retrieved. To measure the resolution length for our preferred model, we defined a series of test models in which we set the isotropic and anisotropic parameters (eqs 2 and 3) to zero except at two selected gridpoints, where we set them to the same arbitrary values. We then computed test data (eq. 7) and inverted it for phase velocity anomalies. Smoothing and damping are as for our preferred model. By varying the distance between the two selected spots and their location on the grid, we estimated the resolution length and its geographical variations. We found resolution lengths of ∼200 km for isotropic anomalies, and ∼300 km for anisotropy anomalies.

5 ISOTROPIC DISPERSION CURVES AND SHEAR WAVE VELOCITY

We inverted the isotropic phase velocity maps locally for radial models of shear wave velocity (V_S). The inversion is a Gauss–Newton gradient search. The V_S-profiles are parametrized with boxcar and triangular basis functions. Given a reference background radial model, the gradient search iteratively updates the model parameters, calculates a synthetic phase velocity curve from the new V_S-profiles, and compares it to the observed dispersion curve. Synthetic phase velocities are calculated following the method of Schwab & Knopoff (1972). The inversion is stopped when the synthetic phase velocity curve fits the observed one with a prescribed precision. Norm damping penalizes deviations from the reference profile. Parameters corresponding to all of the basis functions are damped independently. The depth of the Moho is also a parameter of the inversion. The difference between its inverted and reference (here, crust2.0, http://mahi.ucsd.edu/Gabi/rem.html) values is penalized using an independent damping factor.

We have inverted the isotropic dispersion curve at each gridpoint (red crosses in Fig. 2) for a local radial V_S profile, and assembled these profiles in order to constrain the shear speed structure in this region. At periods larger than 30 s (Fig. 14) our measured dispersion curves are similar to a reference curve computed for an ak135 mantle profile and a region average crustal model accounting for crust2.0. At shorter periods, the measured Rayleigh wave phase velocity are larger than the reference. The difference between the measurement-average and reference phase velocities reaches 150 m s^{-1} at 10 s. Inverted shear wave velocities are higher than those in crust2.0 down to the middle crust, but are indistinguishable from ak135 in the mantle.

In Fig. 15, we plotted the variations in Moho depth and shear wave velocity anomalies (relative to the regional average) that result from our inversions. The distributions in Fig. 15 are affected by three main sources of uncertainties. First, the uncertainties in measured dispersion curves propagate to the V_S-profiles. Second, inversion of the dispersion curve for V_S profiles is sensitive to the applied regularization, and various damping values will result in different profiles. Finally, V_S anomalies in the lower crust and uppermost mantle adjacent to the Moho can trade-off with variations in the Moho depth. Rough estimates of the total uncertainties are ∼3 per cent in V_S anomalies and ∼4 km in the Moho depth. Even accounting for uncertainties of a few kilometres, however, the Moho-depths we inferred are substantially different from those in crust2.0 in this region. The average Moho depth is 41.7 km, that is, more than 3.0 km deeper than in crust2.0. The biggest differences are found in the southeastern part, where the Moho we observe is deeper than that in crust2.0 by about 10 km. The Moho is deeper beneath the orogenic regions (43.4 km) than beneath the central plains (39.7 km). It is shallowest in the southwestern part, in agreement with crust2.0 but with shallower (up to 5 km) values. It is interesting to note that the Moho correlates with surface topography, as expected for Airy isostasy, deepest Moho being found beneath the Appalachian mountain range. The shear wave velocity structure is more uncertain, with amplitude of V_S anomalies comparable or smaller than the estimated uncertainties, except in the upper and middle crust (Fig. 14b).

Comparing radial profiles of the average isotropic anomalies (Fig. 14b) beneath the orogenic terrains (including the Grenville and Appalachian provinces, light blue curve), and beneath the Central Plains (west of the Grenville front, orange curve), we observe that the upper-middle crust is faster than crust2.0 beneath both regions, whereas crustal shear wave velocities are higher beneath Central Plains than beneath the orogenic terrains. This is consistent with the pattern seen in the phase velocity maps at short periods (Fig. 9). In the lower crust, shear wave velocities are close to those in crust2.0 beneath both the Central Plains and the orogenic terrains. Finally, shear velocities beneath the Central Plains and the orogenic terrains are very close to those in ak135 in the lithospheric upper mantle.

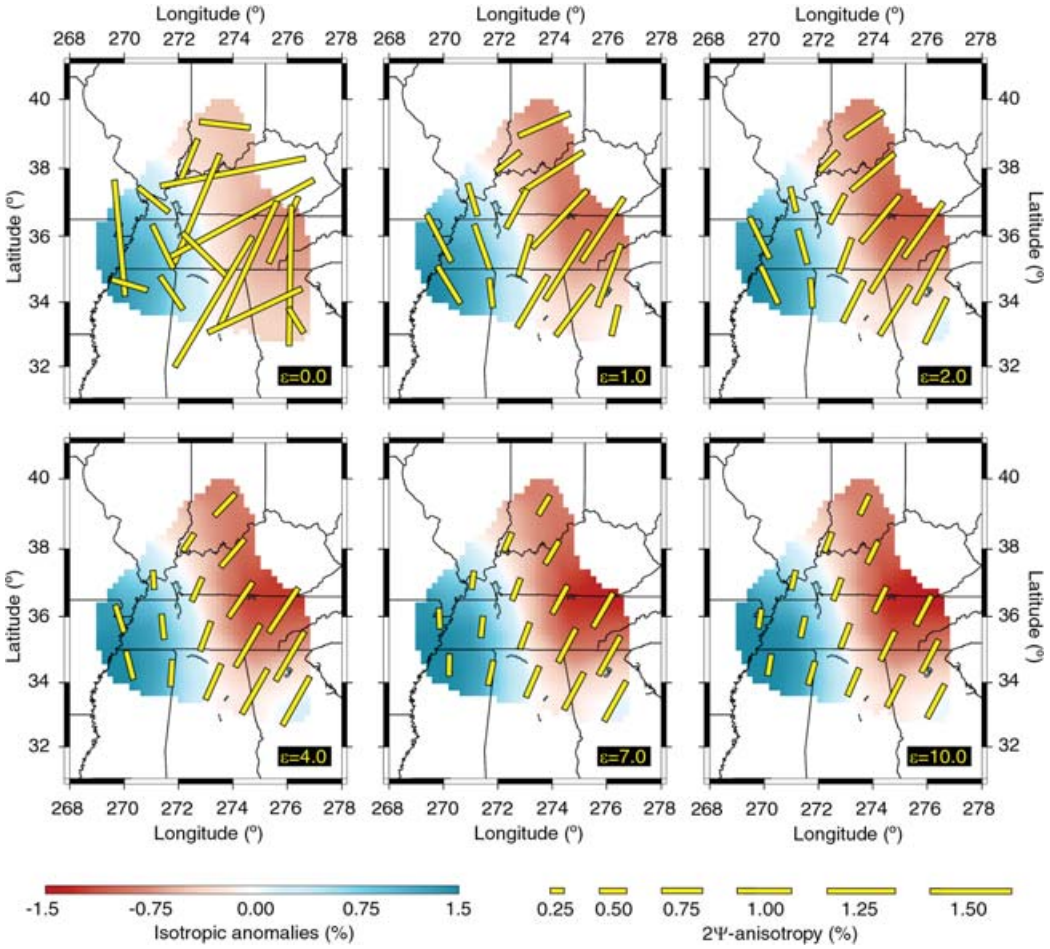

Figure 11. Influence of the 2Ψ-anisotropy smoothing coefficient (ε) on the output model. The smoothing coefficients for isotropic and 4Ψ-anisotropic anomalies are kept constant. The period is $T = 24$ s. At each point, the direction and the size of the bar indicate the direction of the fast axis and the amplitude of the 2Ψ-anisotropic relative anomalies, respectively. The relative isotropic anomalies are also displayed, as indicated by the colour scale.

The grey shaded area in Fig. 14(b) covers twice the estimated uncertainties due to errors in the data. These uncertainties are smaller than the actual uncertainties in V_S because we did not account for the effect of trade-offs between parameters at different depths. Even with these underestimated uncertainties, it is clear that the data do not require that the V_S-profiles in the mantle deviate from ak135.

6 CONCLUDING REMARKS

The main result of this study is the observation of strong anisotropy below east-central US in three distinct period ranges: 20–34, 45–60 and 140–160 s. The amplitude of 2Ψ-term anisotropic anomalies is slightly larger around 140 s than between 20 and 34 s, and the azimuths of the fast-propagation directions in the two period ranges are slightly different from one another. Between 45 and 60 s, anisotropy is smaller in amplitude. Although anisotropy is not required to explain phase–velocity data in this period range, the mapped direction of fast propagation is regionally uniform and perpendicular to that in the period ranges 20–34 and 120–160 s. The anisotropic properties of the mantle layer sampled by Rayleigh wave at 45–60 s are thus distinct from those in the layers above and beneath. In terms of radial structure, our results strongly suggest that azimuthal anisotropy beneath the east-central US is stratified in at least three separate layers. This is in good agreement with recent observations for North America (Marone & Romanowicz 2007).

The azimuths of the fast-propagation directions we inferred in the period range 20–34 s agree very well with those of P_n-anisotropy reported by Smith & Ekström (1999). Smith & Ekström (1999) also observe that azimuthal anisotropy west of the Grenville front is weaker and has a different fast-propagation direction compared to that beneath the Grenville and Appalachian provinces (see their Fig. 11a). The agreement with P_n anisotropy suggests that the anisotropic layer responsible for the phase–velocity anisotropy we observe at 20–34 s includes the uppermost mantle immediately below the Moho. Depth-sensitivity kernels (Fig. 6) predict that this layer may extend from about 25 to 70 km (lowermost crust and uppermost mantle). Interestingly, the azimuth of fast-propagation direction in the Grenville and Appalachian provinces is parallel to the orogenic sutures. Thus, the azimuthal anisotropy we observe in this region is likely the result of deformation during these orogenies, with the anisotropic fabric frozen since then. Both compression and lateral extrusion of the lithospheric roots (Meissner & Mooney 1998; Meissner *et al.* 2002) provide possible mechanisms of deformation. West of the Grenville front, the cratonic Central Plains are likely to have experienced much less deformation during the orogenies, which explains the weaker and less uniform azimuthal anisotropy.

The azimuth of fast-propagation direction we observe at 140 s agrees very well with previously measured direction of shear wave splitting (Barruol *et al.* 1997; Fouch *et al.* 2000), and is also parallel

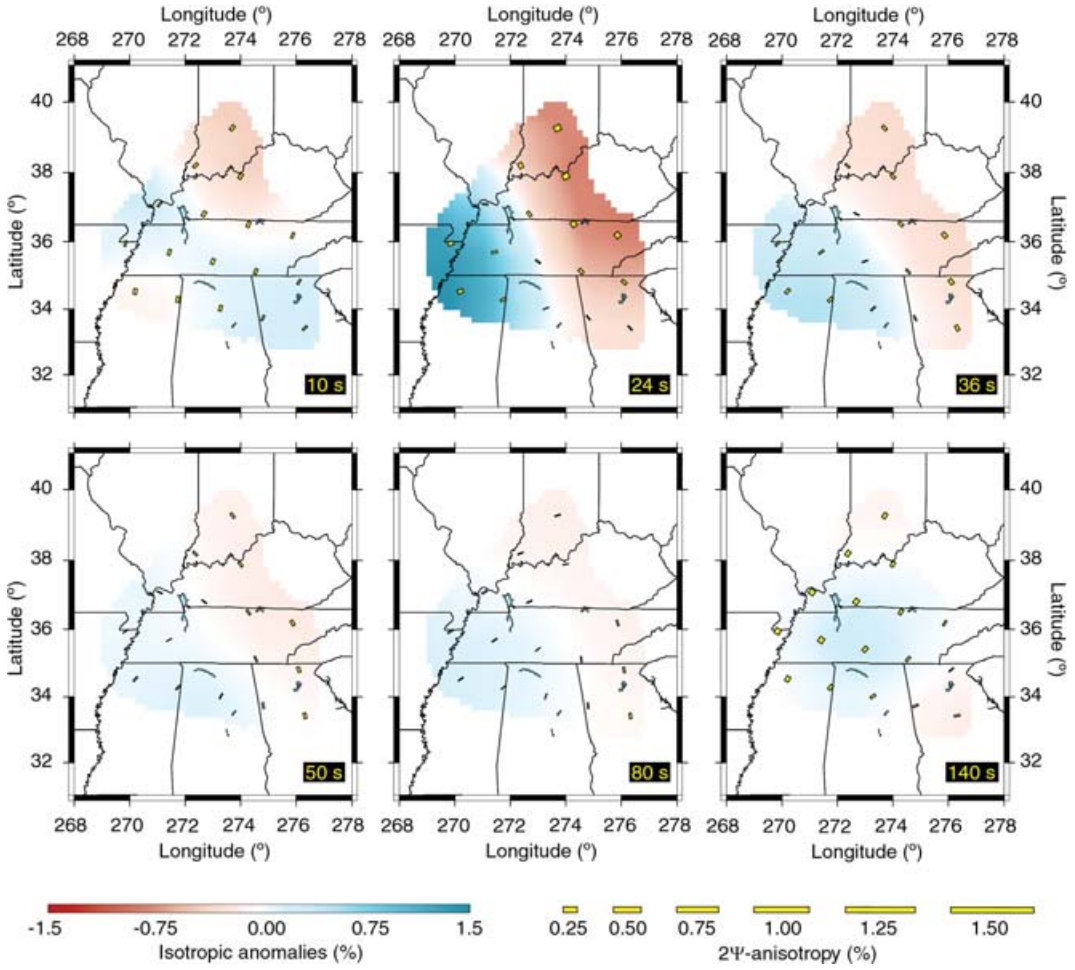

Figure 12. Trade-off between isotropic and anisotropic terms. Input isotropic distributions are those of the preferred model (Fig. 9), and input anisotropic distributions are set to zero. Smoothness coefficients are those of the preferred model.

to the direction of the absolute plate motion predicted by HS2-NUVEL1 (Gripp & Gordon 1990) for the east-central US. The anisotropy observed around 140 s is therefore likely due to current and recent deformation linked to asthenospheric flow. Rayleigh wave sensitivity kernels at these periods indicate that this flow is likely to be located around 150–250 km depth.

Precise estimates of the contribution of each anisotropic layer to the observed shear wave splitting are beyond the scope of this paper. However, we would like to point out that 1–2 per cent of shear velocity anisotropy at 25–70 km (corresponding to the maximum sensitivity range of phase velocity at 20–34 s) would produce shear wave splitting of only 0.1–0.2 s. Phase velocity at 120–160 s sample a thicker layer (say, 150 to 300–350 km depth) and show stronger stronger (1.5 per cent), indicating that shear velocity anisotropy is this layer probably exceeds 2 per cent. This is sufficient to account for the ∼1 s shear wave splitting observed in this region. We thus conclude that most of shear wave splitting observed in the east-central US originates in the asthenosphere.

ACKNOWLEDGMENTS

We are grateful to Gabi Laske, Don Forsyth and an anonymous colleague for their very constructive comments and reviews, which greatly helped to improve the first version of this paper. We also appreciated discussions with Bill Fry and Edi Kissling. This research was partly funded by Utrecht University.

REFERENCES

Barruol, G., Silver, P.G. & Vauchez, A., 1997. Seismic anisotropy in the eastern United States: deep structure of a complex continental plate, *J. geophys. Res.,* **102,** 8329–8348.

Bevington, P.R. & Robinson, D.K., 1992. *Data Reduction and Error Analyses for the Physical Sciences,* McGraw-Hill, New-York.

Fouch, M.J., Fischer, K., Parmentier, E.M., Wysession, M.E. & Clarke, T.J., 2000. Shear-wave splitting, continental keels, and patterns of mantle flow, *J. geophys. Res.,* **105,** 6255–6275.

Freybourger, M., Gaherty, J.B., Jordan, T.H. & the Kaapvaal Seismic Group, 2001. Structure of the Kaapvaal craton from surface waves, *Geophys. Res. Lett.,* **28,** 1109–1112.

Friederich, W. & Huang, Z.-X., 1996. Evidence for upper mantle anisotropy beneath southern Germany from Love and Rayleigh wave dispersion, *Geophys. Res. Lett.,* **23,** 1135–1138.

Gripp, A.E. & Gordon, R.G., 1990. Current plate velocities relative to the hotspots incorporating the NUVEL-1 global plate motion model, *Geophys. Res. Lett.,* **17,** 1109–1112.

Hoffman, P.F., 1988. United Plates of America, the birth of a craton: early Proterozoic assembly and growth of Laurentia, *Ann. Rev. Earth Planet. Sci.,* **16,** 543–603.

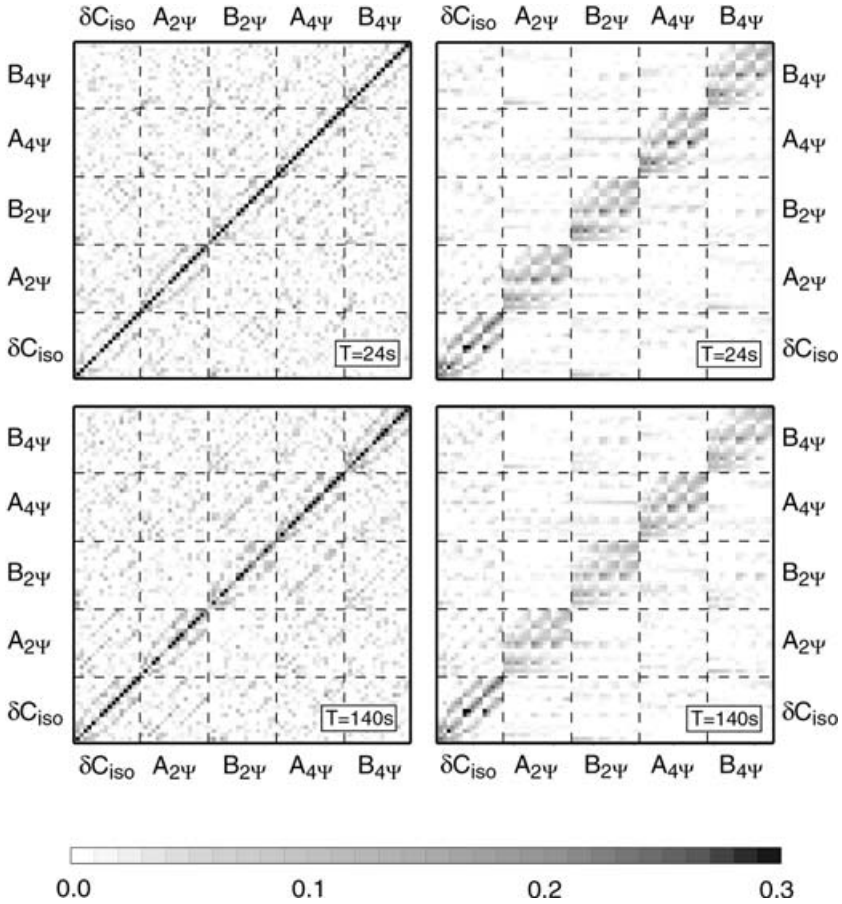

Figure 13. Resolution matrices at 24 s and 140 s without damping and smoothing (left-hand side) and with damping and smoothing similar to those of the preferred model (right-hand side). Each line (column) of the matrix represents a parameter (here, 5 terms at 17 geographical locations, i.e. a total of 85 parameters). For presentation, we separate each matrix in submatrices (dashed lines) of size 17 × 17, that is, that the lines (columns) of the submatrices represent the geographical knots of our model. The diagonal submatrices indicate lateral trade-offs, that is, trade-offs between parameters representing a given term (isotropic anomalies, 2Ψ-anisotropy, or 4Ψ-anisotropy) at different geographical locations. These trade-offs are in large part due to smoothing. The off-diagonal matrices indicate trade-offs between model parameters of different types (isotropic anomalies, and 2Ψ- and 4Ψ-anisotropy terms).

Karlstrom, K.E., Åhäll, K.-I., Harlan, S.S., Williams, M.L., McLelland, J. & Geissman, J.W., 2001. Long-lived (1.8–1.0 Ga) convergent orogen in southern Laurentia, its extension to Australia and Baltica, and implications for refining Rodinia, *Precambrian Res.,* **111,** 5–30.

Kennett, B.L.N., Engdahl, E.R. & Buland, R., 1995. Constraints on seismic velocities in the Earth from traveltimes, *Geophys. J. Int.,* **122,** 108–124.

Knopoff, L., 1972. Observation and inversion of surface-wave dispersion, *Tectonophysics,* **13,** 497–519.

Lebedev, S. & Nolet, G., 2003. Upper mantle beneath southeast Asia from S velocity tomography, *J. geophys. Res.,* **108,** 2048, doi:10.1029/2000JB000073.

Lebedev, S. & Van Der Hilst, R.D. 2008. Global upper-mantle tomography with automated multimode inversion of surface and S wave forms, *Geophys. J. Int.,* in press.

Lebedev, S., Meier, T. & Van Der Hilst, R.D., 2006. Asthenospheric flow and origin of volcanism in the Baikal Rift area, *Earth planet. Sci. Lett.,* **249,** 415–424.

Li, A., Forsyth, D.W. & Fischer, K.M., 2003. Shear velocity structure and azimuthal anisotropy beneath North America from Rayleigh wave inversion, *J. geophys. Res.,* **108,** 2362, doi:10.1029/2002JB002259.

Marone, F. & Romanowicz, B., 2007. The depth distribution of azimuthal anisotropy in the continental upper mantle, *Nature,* **447,** 198–203.

Meier, T., Dietrich, K., Stöckhert, B. & Harjes, H.-P., 2004. One-dimensional model of shear wave velocity for the eastern Mediterranean obtained from the inversion of Rayleigh-wave phase velocities and tectonic implications, *Geophys. J. Int.,* **156,** 45–58.

Meissner, R. & Mooney, W., 1998. Weakness of the lower continental crust: a condition for delamination, uplift and escape, *Tectonophysics,* **296,** 47–60.

Meissner, R., Mooney, W. & Artemevia, I., 2002. Seismic anisotropy and mantle creep in young orogens, *Geophys. J. Int.,* **149,** 1–14.

Montagner, J.-P. & Nataf, H.-C., 1986. A simple method for inverting the azimuthal anisotropy of surface waves, *J. geophys. Res.,* **91,** 511–520.

Montagner, J.-P. & Tanimoto, T., 1991. Global upper mantle tomography of seismic velocities and anisotropies, *J. geophys. Res.,* **96,** 20 337–20 351.

Paige, C.C. & Saunders, M.A., 1982. LSQR: an algorithm for sparse linear equations and sparse least squares, *ACM Trans. Math. Softw.,* **8,** 43–71.

Pedersen, H.A., 2006. Impacts of non-plane waves on two-station measurements of phase velocities, *Geophys. J. Int.,* **165,** 279–287.

Pedersen, H.A., Bruneton, M., Maupin, V. & the SVEKALAPKO Seismic Tomography Working group, 2006. Lithospheric and sublithospheric anisotropy beneath the Baltic shield from surface-wave array analysis, *Earth planet. Sci. Lett.,* **244,** 590–605.

Sato, Y., 1955. Analysis of dispersed surface waves by mean of of Fourier transform: Part. 1, *Bull. Earthquake Res. Tokyo Univ.,* **33,** 33–47.

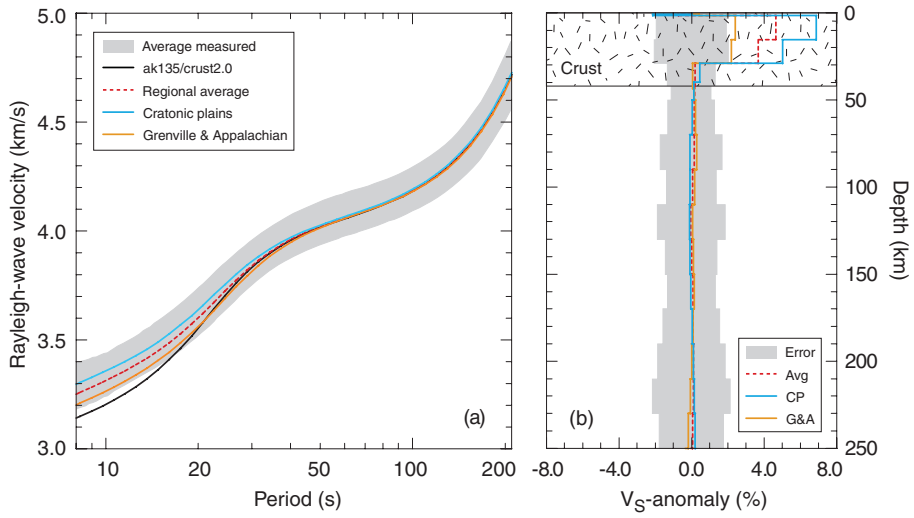

Figure 14. Regional average dispersion curves and shear wave velocity profiles. (a) Dispersion curves. The grey shaded area covers two standard deviations around the regional average over the measured dispersion curves. The black curve is constructed from ak135 (in the mantle) and the regional average of crust2.0 (in the crust). The red dashed curve is constructed from the average of inverted V_S profiles. The orange and blue curves are constructed from the average of inverted V_S profiles beneath the orogenic and cratonic regions, respectively. (b) Profiles of shear wave velocity anomalies relative to ak135/crust2.0. The three profiles represented are the regional average (Avg, red dashed curve), the average profile beneath the Grenville and Appalachian provinces (G&A, orange curve), and the average profile beneath the Central Plains west of Grenville front (CP, blue curve). The grey shaded area covers twice the error bar (defined as the rms of the error due to uncertainties in dispersion curves) around the zero value.

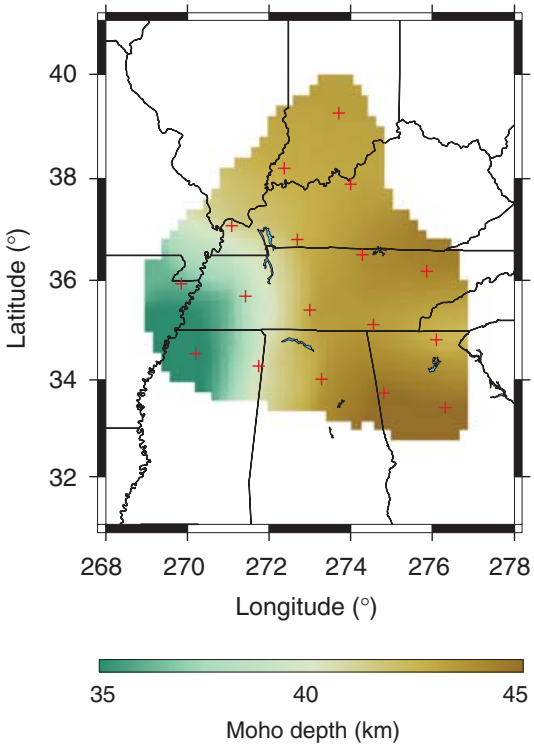

Figure 15. Inverted Moho depth. Red crosses indicate location at which the model is inverted for.

Schwab, F. & Knopoff, L., 1972. Fast surface wave and free mode computations, in *Method in Compotational Physics,* **Vol. 11**, ed. B.A. Bolt, Academic Press, New York.

Sebai, A., Stutzmann, E., Montagner, J.P., Sicilia, D. & Beucler, E., 2006. Anisotropic structure of the African upper mantle from Rayleigh and Love wave tomography, *Phys. Earth planet. Inter.,* **155,** 48–62.

Simons, F.J., Van Der Hilst, R.D., Montagner, J.-P. & Zielhuis, A., 2002. Multimode Rayleigh wave inversion for heterogeneity and azimuthal anisotropy of the Australian upper mantle, *Geophys. J. Int.,* **151,** 738–754.

Smith, M.L. & Dahlen, F.A., 1973. Azimuthal dependence of Love and Rayleigh wave propagation in a slightly anisotropic medium, *J. geophys. Res.,* **78,** 3321–3333.

Smith, G.P. & Ekström, G., 1999. A global study of Pn-anisotropy beneath continents, *J. geophys. Res.,* **104,** 963–980.

Smith, D.B., Ritzwoller, M.H. & Shapiro, N.M., 2004. Stratification of anisotropy in the Pacific upper mantle, *J. geophys. Res.,* **109,** B11309, doi:10.1029/2004JB003200.

Trampert, J. & Lévêque, J.-J., 1990. Simultaneous iterative reconstruction technique: physical interpretation based on the generalized least square solution, *J. geophys. Res.,* **95,** 12 553–12 559.

Trampert, J. & Woodhouse, J.H., 2003. Global anisotropic phase velocity maps for fundamental modes surface waves between 40 and 150 seconds, *Geophys. J. Int.,* **154,** 154–165.

Visser, K., Lebedev, S., Trampert, J. & Kennett, B.L.N., 2007. Global Love wave overtone measurements, *Geophys. Res. Lett.,* **34,** L03302, doi:10.1029/2006GL028671.

Wang, Z. & Dahlen, F.A., 1995. Spherical-spline parameterization of 3-dimensional Earth models, *Geophys. Res. Lett.,* **22,** 3099–3102.

Yang, Y. & Forsyth, D.W., 2006. Rayleigh-wave phase velocities, small-scale convection, and azimuthal anisotropy beneath southern California, *J. geophys. Res.,* **111,** B07306, doi: 10.1029/2005JB004180.

Yoshizawa, K. & Kennett, B.L.N., 2002. Non-linear waveform inversion for surface waves with a neighbourhood algorithm—application to multimode dispersion measurements, *Geophys. J. Int.,* **149,** 118–133.

Ziegler, P.A., 1989. *Evolution of Laurussia: A Study in Late Paleozoic Plate Tectonics,* 102 pp., Kluwer Academic Publishers, Dordrecht.

APPENDIX: GENERALIZED MATRIX

The system of linear equations that we solved to determine the lateral isotropic and anisotropic anomalies assembles a discrete version of eq. (5) for each path, and can be noted

$$\mathbf{d} = G\mathbf{m} \tag{A1}$$

The data vector **d** contains the path-average Rayleigh-wave phase velocity anomaly measured on the dispersion curve at the selected period (see Section 3). The model vector **m** includes five terms (one for isotropic anomalies, 2 for 2Ψ anisotropy, and 2 for 4Ψ anisotropy) for each knot of the grid (eqs 2 and 3). If N is the number of paths available at a given period, and M the number of knots, the transposed data and model vectors are

$$\mathbf{d^T} = (\overline{\delta C}_1 \cdots \overline{\delta C}_N) \tag{A2a}$$

and

$$\mathbf{m^T} = \left(\delta C_{iso,1} \cdots \delta C_{iso,M}\ A_{2\Psi,1} \cdots A_{2\Psi,M}\ B_{2\Psi,1} \cdots B_{2\Psi,M} \qquad A_{4\Psi,1} \cdots A_{4\Psi,M}\ B_{4\Psi,1} \cdots B_{4\Psi,M}\ ,\right) \tag{A2b}$$

respectively. The generalized matrix is composed of five submatrices:

$$\mathbf{G} = \left(\mathbf{G_{iso}} \quad \mathbf{G_{C2\Psi}} \quad \mathbf{G_{S2\Psi}} \quad \mathbf{G_{C4\Psi}} \quad \mathbf{G_{S4\Psi}}\right) \tag{A3}$$

with

$$\mathbf{G_{iso}} = \begin{pmatrix} K_{11} & \cdots & K_{1M} \\ \cdots & \cdots & \cdots \\ K_{N1} & \cdots & K_{NM} \end{pmatrix},$$

$$\mathbf{G_{C2\Psi}} = \begin{pmatrix} a_1K_{11} & \cdots & a_1K_{1M} \\ \cdots & \cdots & \cdots \\ a_NK_{N1} & \cdots & a_NK_{NM} \end{pmatrix}, \quad \mathbf{G_{S2\Psi}} = \begin{pmatrix} b_1K_{11} & \cdots & b_1K_{1M} \\ \cdots & \cdots & \cdots \\ b_NK_{N1} & \cdots & b_NK_{NM} \end{pmatrix},$$

$$\mathbf{G_{C4\Psi}} = \begin{pmatrix} c_1K_{11} & \cdots & c_1K_{1M} \\ \cdots & \cdots & \cdots \\ c_NK_{N1} & \cdots & c_NK_{NM} \end{pmatrix}, \quad \mathbf{G_{S4\Psi}} = \begin{pmatrix} d_1K_{11} & \cdots & d_1K_{1M} \\ \cdots & \cdots & \cdots \\ d_NK_{N1} & \cdots & d_NK_{NM} \end{pmatrix}.$$

In these matrices, the K_{ij} are the weights of path i for knot j (or sensitivity areas), and the azimuthal dependence is accounted for by the constants $a_i = \cos(2\Psi_i)$, $b_i = \sin(2\Psi_i)$, $c_i = \cos(4\Psi_i)$ and $d_i = \sin(4\Psi_i)$, where Ψ_i is the azimuth of the path i.